ORIGINAL ARTICLE

WC–Co/316L stainless steel bonding enhancement by laser surface texturing and pressure-assisted sintering

Liudmila Basílio[1,2] · Bruno Guimarães[1,2] · Óscar Carvalho[1,2] · Cristina Fernandes[3] · Daniel Figueiredo[3] · Filipe Silva[1,2] · Georgina Miranda[4]

Abstract
WC–Co cutting tools are widely used in harsh conditions, but the brittleness of this material can limit their use. Joining steels to WC–Co can provide an alternative, by combining the toughness of steel with the high hardness and wear resistance of WC–Co. The creation of textures at the bonding interface is known to increase the adhesion between materials, through a mechanical interlocking effect and an increase in the contact area. In this sense, this work proposes the laser surface texturing of WC–Co green compacts with cross-hatched and circular micropatterns and subsequent pressure-assisted sintering of the textured and sintered WC–Co with 316L SS powder to improve the bonding between materials. Results showed that the bonding of the textured multi-material was successfully processed and an interdiffusion zone was formed at the bonding interface without the presence of detrimental compounds. The addition of textures showed a tendency to increase the shear bond strength, with the cross-hatched micropatterns generally showing a higher bonding strength than the circular micropatterns. This approach showed to have the potential to improve the bonding between materials, thus contributing to the development of novel multi-material WC–Co/316L stainless steel cutting tools with enhanced properties and performance.

Keywords Multi-material · WC–Co · 316L SS · Cutting tools · Laser surface texturing · Bonding

1 Introduction

Cemented carbides are the most common cutting tool material, being used in more than half of all cutting tools produced worldwide [1]. In the cutting tool industry, the most used cemented carbide is composed of tungsten carbide (WC) as a hard phase and cobalt (Co) as a binder phase, due to a unique combination of high hardness and wear resistance, as well as a good toughness [2–4].

WC–Co tools are widely used in adverse conditions, but due to the brittleness of sintered cemented carbides, the use of these tools may be limited [5]. Joining steels to WC–Co can provide an effective alternative by combining the high toughness of steel with the high hardness and wear resistance of WC–Co, consequently leading to a tool life and fracture toughness increase, at a lower cost [6–8].

A good bond with excellent strength and toughness between steel and WC–Co is not easily achieved due to three factors that severely deteriorate the strength of the bonding joint. These factors include the formation of brittle intermetallic compounds (W_2C, Fe_3W_3C, Fe_6W_6C and Co_3W_3C) at the bonding interface; the dissimilarities in thermal conductivity, which in WC–Co is more than twice that of steel and the uprise of residual stresses due to the coefficient of thermal expansion (CTE) mismatch of WC–Co (5.2 – 6.0×10⁻⁶/°C) [9, 10] and steel (15.9×10⁻⁶/°C) [11], which can generate cracks and defects near the interface [12–17].

Different manufacturing techniques have been used to bond steels to WC–Co, namely brazing [7, 18], laser welding

---

Filipe Silva and Georgina Miranda are Co-last authorship.

✉ Bruno Guimarães
brunopereiraguimaraes@hotmail.com;
bguimaraes@dem.uminho.pt

1 Center for MicroElectroMechanical Systems (CMEMS-UMinho), University of Minho, Campus de Azurém, 4800-058 Guimarães, Portugal

2 LABBELS – Associate Laboratory, Braga/Guimarães, Portugal

3 Palbit S.A., P.O. Box 4, 3854-908 Branca, Portugal

4 CICECO, Aveiro Institute of Materials, Department of Materials and Ceramic Engineering, University of Aveiro, 3810-193 Aveiro, Portugal

[19, 20], diffusion bonding [10, 21, 22], sinter bonding [23, 24], among others [17, 25, 26]. Brazing has been explored for bonding WC–Co and steel, through the use of filler metals, such as Ni-based, Cu-based, or Ag-based alloys. However, brazed joints may present limitations at high temperatures, due to a low thermal resistance [8, 27]. Laser welding can also be used, although some reported problems, as the introduction of large amounts of brittle phases, due to a strong reaction at the interface and/or the formation of significant residual stresses in the joint, due to the rapid solidification of the weld line, thus leading to fracture of the multi-material under low pressures [8]. Diffusion bonding is a technique that produces solid-state coalescence between two materials. In this technique, plastic deformation and interdiffusion of elements along the bonding interface promote joints with greater strength and toughness [8, 28]. For joining WC–Co and steel by this technique, intermediate layers such as Cu, Ag, or Ni are usually used to reduce the CTE mismatch between bonding materials [28].

Sinter bonding or sintering is one of the most used powder metallurgy processing techniques for bonding cemented carbide to other materials, mainly due to its relatively simplicity and low cost, through particle rearrangement and diffusion processes [28, 29]. Wang et al. [23] used this technique to join WC-20wt.%Co to Fe-36wt.%Ni powder at 1300 °C for 2, 8, and 16 h under vacuum. Results showed that a consolidated interface comprised primarily of hexagonal α-WC, cubic $Fe_{0.64}Ni_{0.36}$ and Co_3W_3C, whose content increased as a function of holding time. Prolonged holding times promoted bonding of the WC–Co/Fe–Ni component, but excessive holding times resulted in significant contractions and failure by cracking. Also, the increase in holding time led to a grain size increase. Maizza et al. [24] proposed a new solid-state capacitor discharge sinter-welding to bond WC–12Co and AISI M2 steel. This process allows very short processing times, which help to prevent the coarsening of steel grains or WC particles, as well as avoid WC decomposition and minimized microstructural defects, being successfully achieved the bonding of the two joining materials. Pressure-assisted sintering or hot pressing (HP) is a technique that consists in applying simultaneously pressure and temperature, which accelerates the densification kinetics, thus allowing to obtain highly densified final products with fewer structural defects, such as voids or microcracks. Furthermore, it allows the production of components with controlled microstructure [30, 31].

Moreover, surface topography has a strong influence on the bond between materials, as some studies have shown [32–35]. Wagner et al. [36] and Henriques et al. [37] studied the influence of roughness on the adhesion of a metal-ceramic system and concluded that surface roughness at the metal-ceramic interface plays an important role in the formation of a strong bond, due to the surface area increase,

where chemical bonds can be established, and the creation of a non-linear fracture path, which in turn increases the surface area of the fracture and the energy required for failure. Li et al. [38] performed a numerical analysis to obtain the thermal history of different groove shapes on the laser welding-brazing of aluminium to steel. It was found that the smallest temperature gradient along the steel interface was noticed at the half V-shape groove joint, thus leading to the highest tensile strength.

Laser surface texturing has been increasingly used for surface modification, due to being a non-contact operation mode that allows high-precision production of various geometries, including complex shapes and details with thicknesses of less than 200 μm [39, 40]. Thus, the combination of pressure-assisted sintering and laser surface texturing emerges as a potential strategy for joining WC–Co and steel.

In this context, this study aims to improve the bonding between WC–Co and 316L stainless steel, without the addition of an interfacial layer, through laser surface texturing of WC–Co green compacts with cross-hatched and circular micropatterns that are subsequently sintered and afterwards bonded through pressure-assisted sintering of the textured and sintered WC–Co compacts with the 316L SS powder. To the author's best knowledge, this study is the first proposing the use of laser surface texturing for enhancing the bonding strength between WC–Co and steel, thus contributing to the development of novel multi-material WC–Co/316L stainless steel cutting tools with enhanced properties and performance.

2 Materials and Methods

2.1 Laser surface texturing of green compacts

WC and Co powders supplied by Palbit S.A. with an average particle size of 0.8 μm and 1.5 μm, respectively, were used to prepare a powder mixture of WC-10wt%Co. This powder mixture was homogenized with 2 wt% paraffin in a ball mill for 48 h, followed by drying and sieving, resulting in granules with a tendentially spherical shape and a D50 of 200 μm. Figure 1 a) and b) shows a SEM image of the WC–Co powder and its granulometric distribution, respectively. An X-ray diffraction analysis was performed on WC-10wt%Co powders and the obtained diffraction pattern is shown in Fig. 2.

To produce WC-10wt%Co green compacts, compaction was carried out by applying a uniaxial pressure of 200 MPa for 30 s, resulting in compacts of cylindrical shape with 12 mm diameter and 4.5 mm thickness.

After production of the green compacts, laser surface texturing was performed by using an Nd:YAG laser (wavelength of 1064 nm) with a maximum working power of 6 W and a laser spot size of 3 μm. The laser beam was focused on the green compacts surface at a focal length of 160 mm.

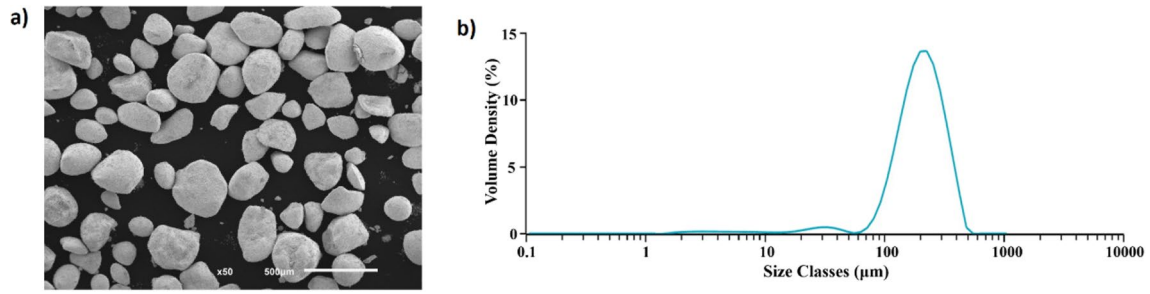**Fig. 1** WC–Co powder: **a**) SEM image and **b**) particle size distribution
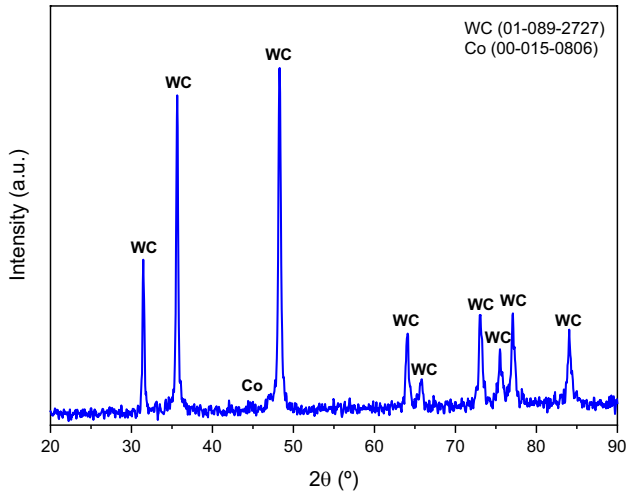

Fig. 2 X-ray diffraction pattern of WC–Co powder

During and after texturing, an air jet was applied to remove the debris produced during the texturing process.

In this study, two micropatterns were produced, cross-hatched and circular. To vary the bonding area between WC–Co and 316L SS, in all textures, the groove width and depth were varied. Regarding the peak width/diameter, it was kept constant in all experiments. The dimensions of the textures were selected considering the granulometry of the steel powder and existing literature [41, 42]. Figure 3 shows a schematic representation of the patterns designed for this study and in Table 1 their intended dimensions are presented.
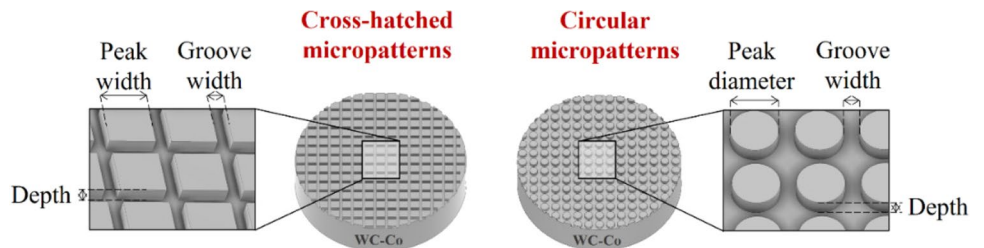
Table 1 Cross-hatched and circular micropatterns dimensions

Experiment	Peak width/diameter (µm)	Groove width (µm)	Depth (µm)
I	150	150	150
II			200
III		200	150
IV			200
V		250	150
VI			200

To achieve the desired width of the grooves, multiple scan lines were used with a 10 µm space between them, until reaching the desired width. For texturing of the cross-hatched micropatterns, the same laser parameters used in the study by Guimarães et al. [43] were used. On the other hand, for laser surface texturing of the circular micropatterns, optimization was carried out, which led to the conclusion that to obtain well-defined circular micropatterns, it is necessary to use different parameters in the peaks and grooves. In addition, an optimization of the number of passages was also performed, to reach the desired depths. Table 2 shows the laser parameters used for laser surface texturing of the cross-hatched and circular micropatterns and in Fig. 4 a schematic representation of the texture design is shown.

2.2 Dewaxing and Sintering

After laser surface texturing of the WC–Co green compacts, dewaxing and sintering were carried at Palbit S.A. according to their specifications. Dewaxing was performed at 600 °C in a hydrogen atmosphere and sintering at 1480 °C in a SinterHIP furnace, under argon atmosphere, at 20 bar.

Fig. 3 Schematic representation of cross-hatched and circular micropatterns

Table 2 Laser processing parameters used for laser surface texturing of cross-hatched and circular micropatterns

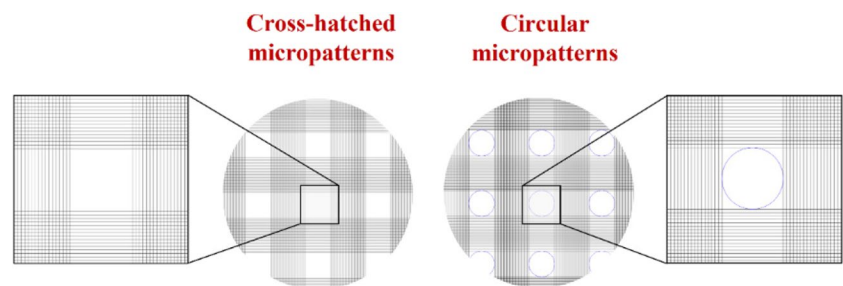| Micropattern		Laser power (W)	Scan speed (mm/s)	Number of passages (N)
Cross-hatched	Peaks and grooves	1.50	256	4 and 6
Circular	Grooves	1.50	256	4 and 6
	Peaks	0.78	10	

2.3 316L SS HP processing optimization

In this study, 316L stainless steel powders from LPW Technology Ltd were used. This powder has a spherical shape with a D50 particle size of 28.8 μm, as seen in Fig. 5 a). The X-ray diffraction pattern of the 316L SS powder is shown in Fig. 5 b).

Once the WC–Co compacts were textured and sintered, it was necessary to perform an optimization of the hot pressing parameters to obtain the best mechanical properties for 316L SS. For this optimization a sintering temperature of 1100 °C, a pressure of 45 MPa and a sintering time of 15 min and 30 min were studied, being these parameters defined considering the study carried out by Bartolomeu et al. [44].

To process the 316L SS specimens by HP, 2.2 g powder was used, thus being obtained specimens with final dimensions of 10 mm diameter and 3.5 mm thickness. The processing was carried out by uniaxial hot pressing, using an

induction furnace, assisted by a hydraulic press, and coupled to a primary vacuum pump. HP processing begins with the introduction of the powders in a graphite mould, being then taken to the HP oven where it is heated under vacuum (10^{-2} mbar), up to 1100 °C. At 1100 °C, the pressure is applied gradually and when the selected temperature is reached, the desired pressure is applied and maintained during the sintering time. After the end of the cycle, heating is suspended, and the specimen is cooled inside the oven in vacuum until it reaches room temperature.

2.4 Multi-material WC–Co/316L SS processing

Multi-material specimens' production starts with the selection of the best 316L SS HP processing parameters. Before the fabrication by HP, the WC–Co parts (textured and sintered) were ultrasonically cleaned for 30 s in propanol.

The amount of 316L SS powder used at this stage was the same that was used in the 316L SS processing optimization stage. Firstly, the WC–Co part (textured and sintered) is introduced into a graphite mould and then the 316L SS powder is introduced on top of the WC–Co part. For comparison purposes, untextured and sintered WC–Co parts were also bonded to 316L SS (control specimens). Figure 6 shows a schematic representation of the arrangement of the two materials inside the graphite mould.

After the bonding process, it is necessary to carry out a surface preparation, which aims to remove the excess of steel,

Fig. 4 Schematic representation of the cross-hatched and circular micropatterns texture design (not to scale). The black and blue lines represent the laser passages with different parameters and the white areas represent the untouched areas

Fig. 5 316L SS powder: **a**) SEM image and **b**) X-ray diffraction pattern

so that the multi-material bonding interface is perfectly visible for its characterization. This preparation consists of grinding with 180 and 320 mesh polishing sandpapers. Finally, the specimens were ultrasonically cleaned for 30 s in propanol. After this process, the multi-material specimen had a cylindrical shape with a 10 mm diameter and 6.7 mm thickness.

2.5 Topographical and crystallographic characterization

Scanning electron microscopy (SEM) was used to evaluate the microstructure and topography of the textured cross-hatched and circular micropatterns, and the fracture surface of the multi-material specimens after shear tests. For this characterization, the equipment JEOL JSM-6010L was used, to which an energy dispersion spectroscopy (EDS) equipment is attached.

After laser surface texturing and sintering, to evaluate the topography and dimensions of the textures, 3D optical profilometry was performed. This analysis was performed on a Sensofar S-neox profilometer, according to the ISO 25178 (2012) standard, coupled to a SensoSCAN software. For depth measurement, six measurements were performed on each specimen.

To evaluate the influence of the laser on the textured WC–Co green compacts, namely regarding the formation of new compounds, XRD analyses were performed on the specimens that suffered the highest laser interaction. Furthermore, after the shear tests, XRD analyses were also performed to assess the presence of compounds resulting from the diffusion between 316L SS and WC–Co on the fracture surfaces of the multi-material. For this analysis, a Bruker D8 Discover diffractometer was used with Cu-kα radiation ($\lambda = 1.5418$ Å) in $\theta/2\theta$ mode, range 20° to 90°, step of 0.05° and an integration time of 1 s.

2.6 Hardness measurements and shear tests

To determine the best processing parameters for 316L SS, Vickers macro hardness tests were executed, with six indentations performed for each condition, by applying 30 kgf for 20 s. These tests were performed on an Officine Galileo D200 hardness tester.

Shear tests were carried out on 316L SS specimens to assess the best processing condition to achieve the higher mechanical strength for this material and to verify the shear bond strength of the multi-material, being performed at room temperature on INSTRO874 MA equipment under a crosshead speed of 0.002 mm/s. For 316L SS shear tests, two specimens were tested for each sintering time and for multi-material shear tests four specimens were tested for each micropattern experiment. The shear tests on the 316L SS specimens were performed in a custom-made stainless steel apparatus similar to that described by Miranda et al. [45]. As shown in Fig. 7 a), this device essentially consists of a sliding part equipped with a cutting tool. On the sliding part, a downward force is applied to the upper part until fracture of the specimen due to shear loading.

For the multi-material specimens, tests were performed in a specially developed custom-made stainless-steel apparatus consisting of a fixed and a sliding part, each with two aligned holes for the insertion of the specimen. After inserting the specimen, an adjustment screw was used to position the specimen, aligning the multi-material interface (WC–Co/316L SS) with the sliding plane of fixed and sliding parts. On top of the sliding part, a downward force is applied until fracture due to shear loading (see Fig. 7 b)). The shear strength of 316L SS and the shear bond strength of the multi-material were determined by dividing the maximum force (N) recorded by the cross-sectional area of the specimens (mm²).

3 Results and Discussion

3.1 Characterization of textured surfaces

As previously mentioned, in this study cross-hatched and circular micropatterns were produced on the WC–Co green compacts surface, with the intended dimensions shown in Table 1 and produced with the laser parameters presented in Table 2. SEM images of the sintered WC–Co laser textured surfaces are shown in Fig. 8.

Fig. 6 Schematic representation of the arrangement of the two materials inside the graphite mould
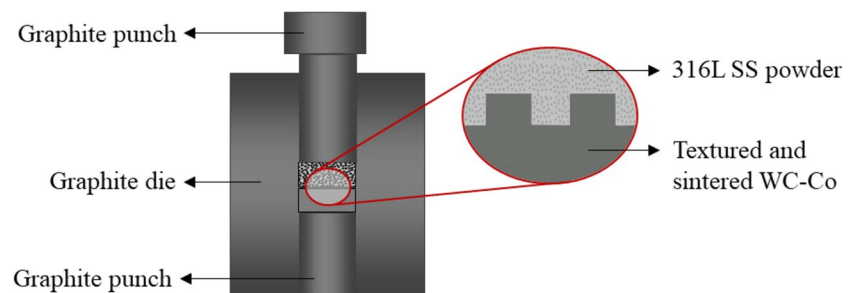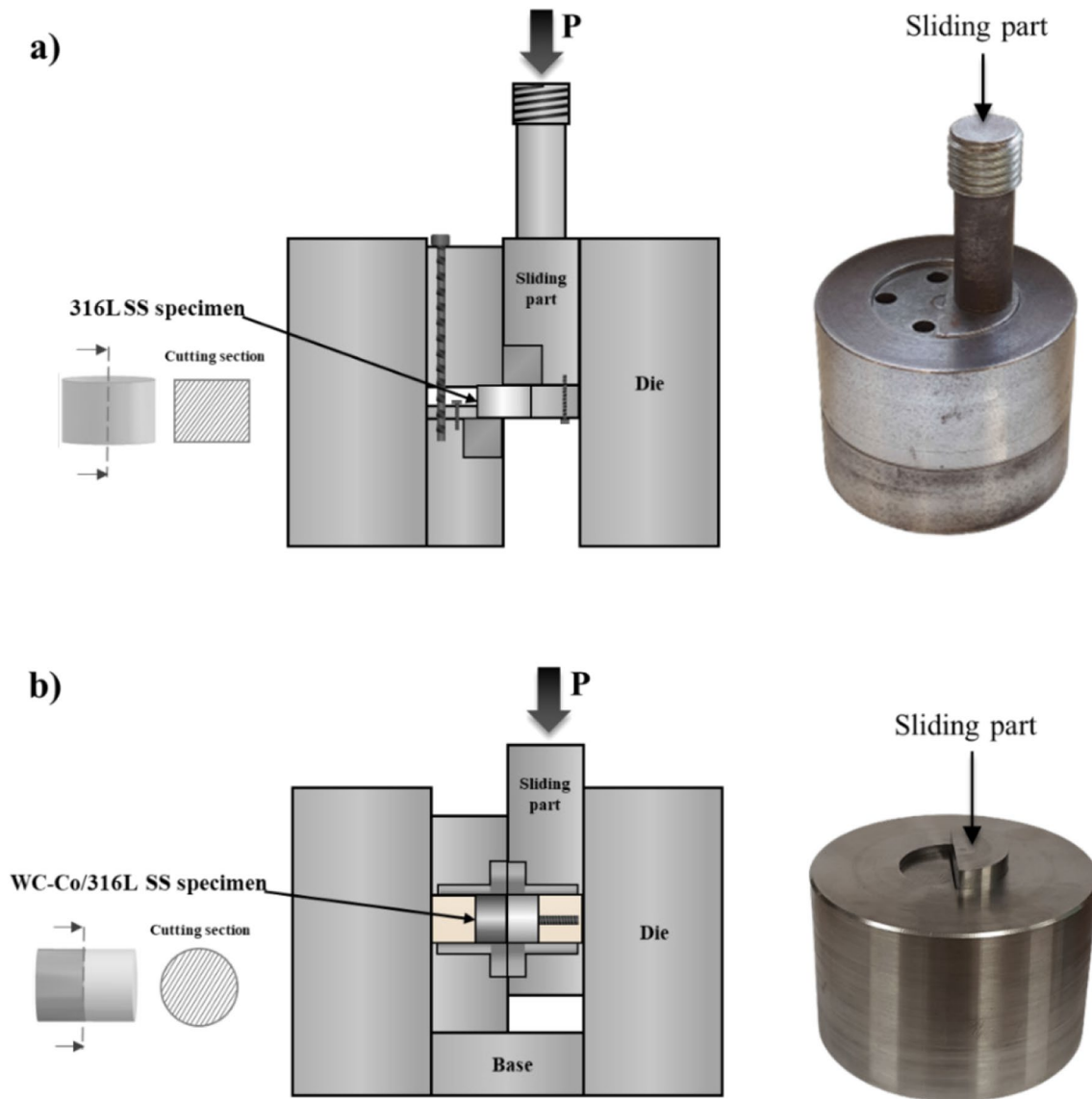
Fig. 7 Schematic representation of the shear test operation and custom-made apparatus used to perform the tests: **a**) 316L SS specimens shear test and **b**) multi-material specimens shear test

By analysing Fig. 8 it is possible to verify that the produced textures, both the cross-hatched and the circular micropatterns, are well-defined (non-distorted), reproducible, and equally spaced. The well-defined circular micropatterns were performed using lower laser power and scan speed in the peaks, when compared to that used for the grooves. Furthermore, no microcracks, spatter and severely heat affected areas were observed on the textured parts, aspects that could compromise the integrity and mechanical strength of the WC–Co textured parts. This demonstrates the effectiveness of laser surface texturing on green WC–Co compacts, as reported in other studies [40, 43].

To evaluate the laser influence on the textured WC–Co green compacts, X-ray diffraction analyses were carried out on the specimens (after sintering) that suffered greater laser

interaction. In this way, WC–Co compacts with higher texture density and a higher number of laser passages were selected (experiment II). Figure 9 shows the X-ray diffraction patterns of these experiments and of the WC–Co powder.

When analysing Fig. 9, it is possible to observe that the XRD peaks of the cross-hatched and circular micropatterns coincide with the WC and Co characteristic peaks, being no other phases detected. In the XRD pattern of WC–Co powder, the characteristic peak of cobalt is not perceptible due to the presence of paraffin wax and some amorphization. These analyses allow to conclude that laser surface texturing of cross-hatched and circular micropatterns with the highest number of passages did not lead to the formation of carbon deficient phases, such as W_2C, Co_3W_3C, and Co_6W_6C or

Fig. 8 SEM images of textured and sintered WC–Co parts with cross-hatched and circular micropatterns
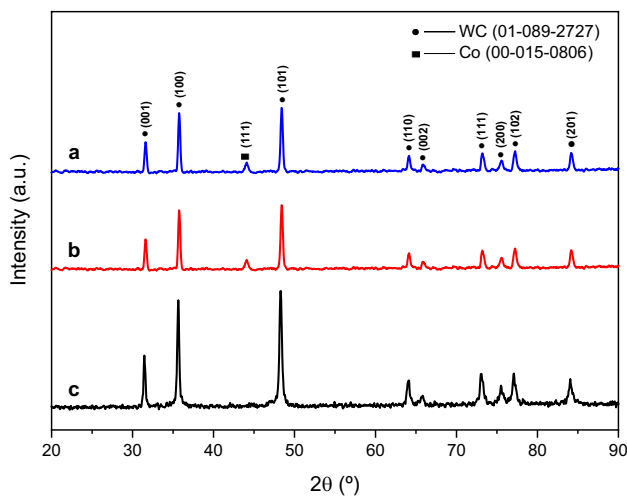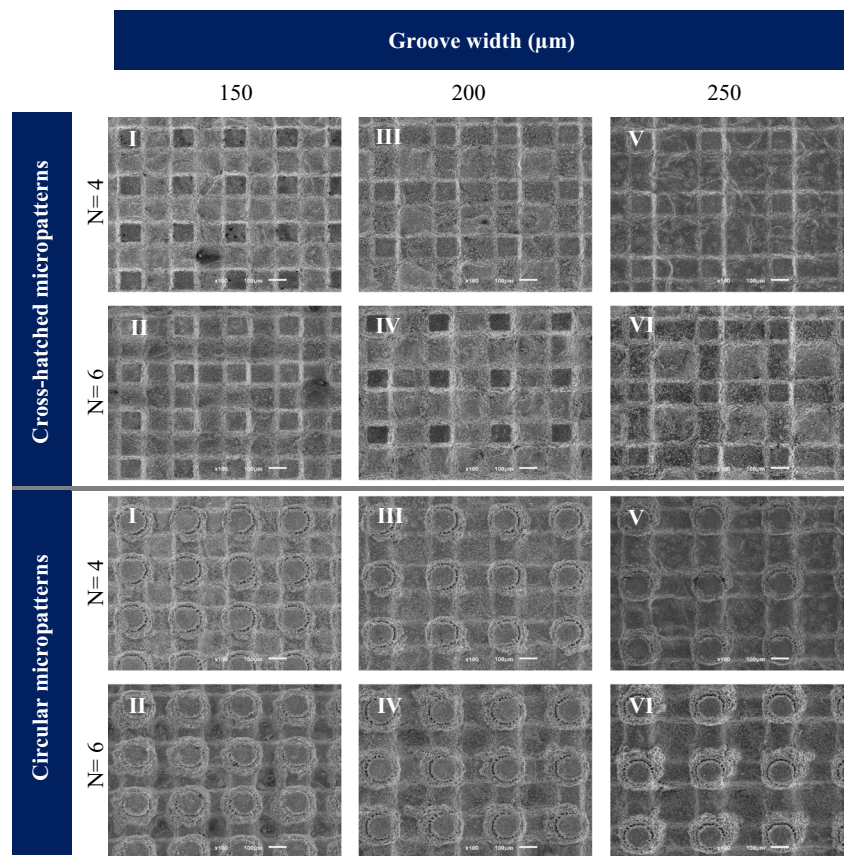
Fig. 9 X-ray diffraction patterns of WC–Co: **a**) textured and sintered cross-hatched micropatterns (experiment II); **b**) textured and sintered circular micropatterns (experiment II) and **c**) WC–Co powder
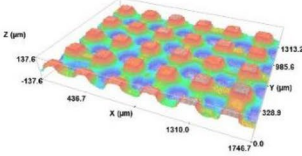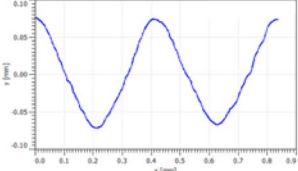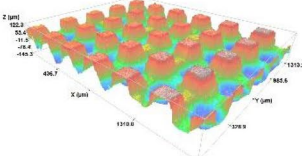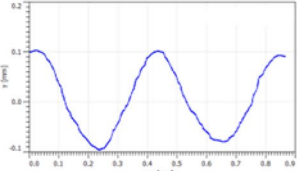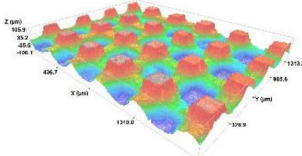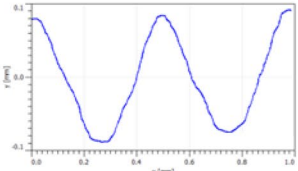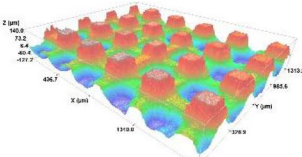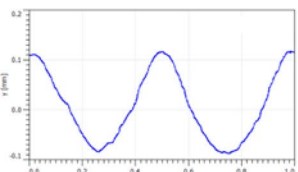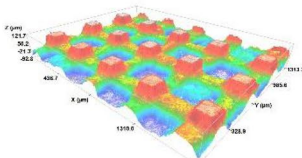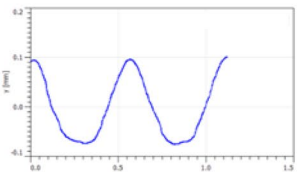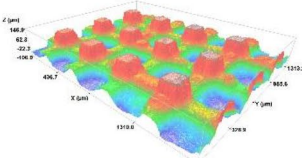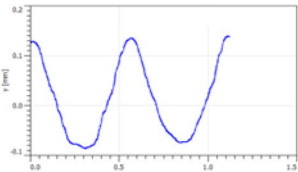

free carbon, which would significantly affect the mechanical properties of WC–Co [46]. Since there is no formation of detrimental phases in these specimens, it is expected that there is no formation of these phases in the other specimens, as they suffered a lower laser interaction.

After sintering, 3D optical profilometry was performed to evaluate the topography, roughness, and dimensions of the produced textures. Tables 3 e 4 show the 3D images, surface roughness values (according to the ISO 25178 (2012) standard) and a representative profile of the WC–Co surfaces for cross-hatched and circular micropatterns, respectively.

In Tables 3 and 4, two values of surface roughness are presented, Sa, which represents the average surface roughness and Sq, which represents the root mean square. For both cross-hatched and circular micropatterns, Sa values increase with the number of passages, due to the increase in textures depth (experiments I and II, III and IV, and V and VI). In turn, it can be observed that in all textures the Sq values are higher than the Sa values. This is due to a greater sensitivity of Sq to a large deviation from the mean line, when compared to Sa. As an example, a large peak or valley on the surface leads to a greater increase in Sq than in Sa. Furthermore, it is possible to notice in the micropattern profiles that laser surface texturing produced textures with a sinusoidal profile, due to the non-uniform energy distribution of the laser beam, which follows a Gaussian distribution, that is, the maximum intensity of the beam laser is located in the centre of its diameter and falls radially to its lowest intensity [43].

Using 3D optical profilometry and Gwyddion software, the dimensions of cross-hatched and circular micropatterns

Table 3 3D optical profilometry images, surface roughness values, and micropattern profiles for cross-hatched micropatterns (after sintering)

Experiment	3D images	Surface roughness	Micropattern profiles
I		S_a= 37.12 μm S_q= 45.89 μm	
II		S_a= 53.73 μm S_q= 64.97 μm	
III		S_a= 38.75 μm S_q= 48.71 μm	
IV		S_a= 49.96 μm S_q= 62.71 μm	
V		S_a= 37.06 μm S_q= 46.96 μm	
VI		S_a= 49.60 μm S_q= 62.12 μm	
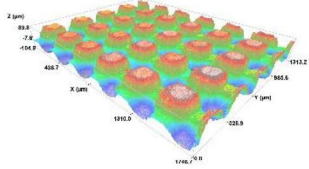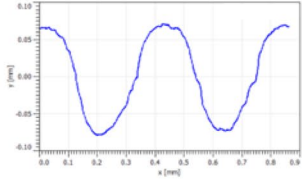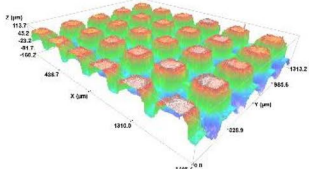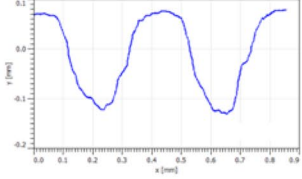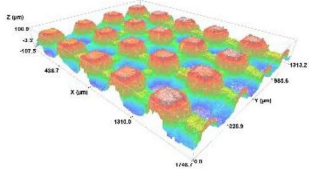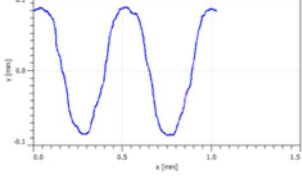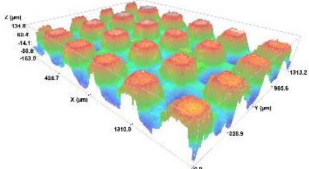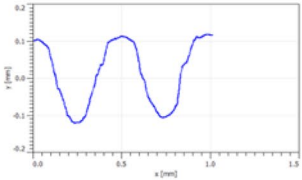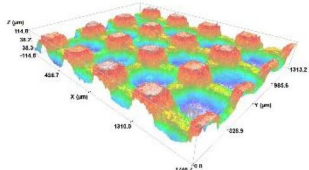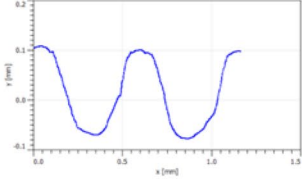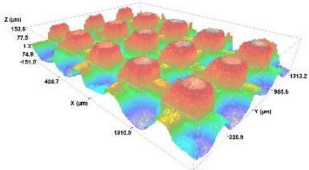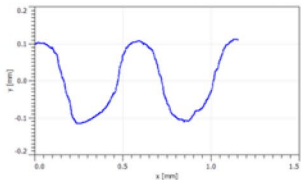
were determined after laser surface texturing and sintering of WC–Co compacts. The obtained dimensions are shown in Table 5, where it is possible to perceive that the cross-hatched and circular micropatterns present different dimensions, i.e. compared to circular micropatterns, the cross-hatched micropatterns have a smaller peak width and consequently a larger groove width. This different outcome

may be associated with the different strategies (laser path) used for each design. In this case, for texturing the circular micropatterns, the same strategy used for the cross-hatched micropatterns was employed and afterwards the circles were textured.

From Table 5 it is also possible to verify, in all textures, that an increase in the number of passages leads to a depth

Table 4 3D optical profilometry images, surface roughness values, and micropattern profiles for circular micropatterns (after sintering).

Experiment	3D images	Surface roughness	Micropattern profiles
I		S_a = 45.80 µm S_q = 51.71 µm	
II		S_a = 63.38 µm S_q = 70.77 µm	
III		S_a = 44.02 µm S_q = 51.71 µm	
IV		S_a = 68.50 µm S_q = 78.41 µm	
V		S_a = 46.98 µm S_q = 56.78 µm	
VI		S_a = 66.17 µm S_q = 80.03 µm	

increase, as expected, since more energy is irradiated into the same area. Furthermore, for the same number of passages, textures with wider grooves have higher depths. This increase in depth is related to the laser affected area, since to create wider grooves is necessary to have more laser passages to remove material, thus resulting in a larger laser affected area.

3.2 316L SS HP processing optimization

For the multi-material fabrication, firstly it was necessary to optimize the 316L SS HP processing parameters. To evaluate the best processing condition, hardness and shear tests were performed on 316L SS specimens, processed with the parameters described in the Sect. 2.3. For 15 min

Table 5 Cross-hatched and circular micropatterns dimensions after laser texturing and sintering

Experiment		Peak width (µm)	Groove width (µm)	Depth (µm)
Cross-hatched micropatterns	I	113.78 ± 2.34	182.65 ± 3.67	142.38 ± 4.34
	II	113.94 ± 1.24	180.66 ± 4.06	200.64 ± 6.35
	III	112.30 ± 3.69	231.98 ± 3.52	151.44 ± 8.56
	IV	115.46 ± 3.59	227.67 ± 3.98	199.68 ± 12.47
	V	112.26 ± 2.19	282.97 ± 2.83	161.92 ± 9.41
	VI	114.17 ± 2.43	282.53 ± 3.71	211.20 ± 9.36
Circular micropatterns	I	131.71 ± 2.54	164.36 ± 2.63	140.57 ± 4.77
	II	129.73 ± 2.93	166.18 ± 3.64	187.93 ± 10.60
	III	127.74 ± 3.25	216.92 ± 2.80	152.57 ± 11.13
	IV	126.38 ± 3.14	218.16 ± 2.88	219.71 ± 10.24
	V	122.33 ± 2.82	269.79 ± 3.14	177.06 ± 5.80
	VI	127.97 ± 2.61	266.54 ± 3.76	225.29 ± 18.60

of sintering time, a hardness of 164 ± 8 HV30 and a shear strength of 472 ± 12 MPa were obtained. On the other hand, for 30 min of sintering time, it was obtained 186 ± 17 HV30 of hardness and 503 ± 9 MPa of shear strength. The higher hardness and shear strength obtained when 30 min of sintering time was used indicate a possible higher densification, due to the longer sintering time.

In a study carried out by Bartolomeu et al. [44], 316L SS was processed by HP with processing conditions similar to those used in this work, differing in the applied pressure (44 MPa). In the present study, an applied pressure of 45 MPa led to a hardness of 176 HV3. In another study carried out by Cunha et al. [47], 316L SS was processed by HP at 900 °C for 30 min with a pressure of 70 MPa, obtaining a hardness of 185 HV30. Although similar, these differences in hardness can be acceptable due to the different pressures and/or sintering time and temperature, that lead to different densification levels.

To sum, it was possible to conclude that the best HP processing condition for 316L SS are 30 min of sintering time, 45 MPa of pressure, at a temperature of 1100 °C, being these the conditions selected for multi-material WC–Co/316L SS processing.

3.3 Shear bond strength

To evaluate the shear bond strength of the multi-material, shear tests were carried out at the multi-material interface, with Fig. 10 showing a typical stress–strain curve and the results of the shear bond strength of the multi-material. As seen in Fig. 10, the multi-material fracture can essentially be divided into three stages. Stage I is characterized by the presence of some elastic deformation of the material, accommodation of the material to the shear test device and low stresses that slowly increase. Then, stage II takes place, being defined by the presence of plastic deformation and

the development of cracks with increasing stress. Finally, stage III, in which the maximum stress is reached and failure occurs [48].

Control specimens present a shear bond strength of 30 ± 14 MPa and despite the high deviations, the results of multi-material with micropatterns show a tendency to increase the shear bond strength compared to the untextured control. These deviations may be explained by different texture orientations along the shear plane during the shear tests. In general, cross-hatched micropatterns display a higher shear bond strength than circular micropatterns. More insights on the reasons for this phenomenon will be given in the next section. Comparing to other studies found in literature for the same and similar bonding techniques, the obtained shear bond strength was found to be in good agreement [17, 22].

Regarding the influence of texture dimensions on the shear bond strength, it seems that deeper micropatterns have the tendency to originate multi-material specimens with lower shear bond strength (e.g. cross-hatched micropatterns experiment I and II, and circular micropatterns experiment V and VI).

Overall, it can be concluded that the addition of textures at the bonding interface shows a tendency to increase the shear bond strength, mainly due to three factors. The addition of surface roughness plays a key role in the bonding between materials, being known to be one of the most effective strategies for improving bond strength due to the mechanical interlocking effect. Also, the larger surface area of a rough surface allows chemical bonds to be established, contributing to the formation of a stronger bonding. Finally, the non-linear fracture path, which in turn increases the surface area of the fracture and the energy required for failure, enhances the bond strength. In this way, the combination of mechanical and chemical bonds plays an important role in the formation of a strong bond. [36, 37].

Fig. 10 Stress–strain characteristic curve of the multi-material shear test and multi-material shear bond strength (control, cross-hatched micropatterns, and circular micropatterns)
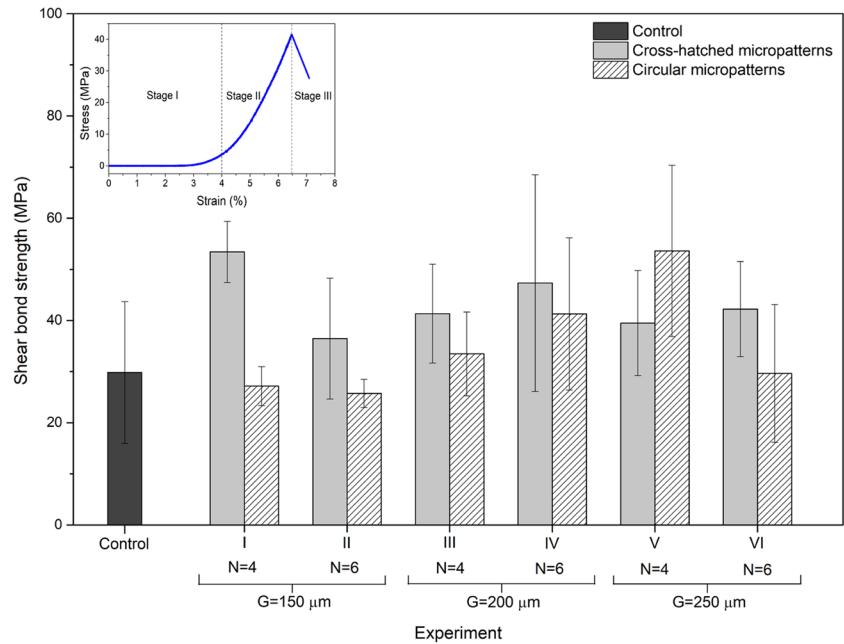
3.4 Fracture surface and bonding interface analysis

After shear tests, the fracture surfaces of the multi-material specimens were examined by SEM, to evaluate the failure mode of the multi-material. Figure 11 shows SEM images of the different fracture surfaces, namely control, cross-hatched micropatterns, and circular micropatterns. When analyzing Fig. 11, it is possible to identify the starting point of the fracture and its propagation direction, on all the surfaces. In Fig. 11 a) the fracture surface of the control multi-material is smoother and characterized by the presence of some micro-voids, also known as dimples. These voids have a parabolic shape that extends in the opposite direction to the loading direction, which suggests a ductile fracture of the multi-material [49]. On the other hand, the fracture surfaces of textured multi-materials (Fig. 11 b) and c)) present a more irregular topography, due to more energy being needed to reach the rupture, which in turn is promoted by the mechanical interlocking effect of the textures at the bonding interface. In Fig. 11 b) and c) the fracture surfaces are characterized by the presence of several fracture planes, which suggests a brittle fracture by cleavage. The formation of these fracture planes may be due to the change in the paths of the microcracks during the propagation of the fracture, due to the presence of textures [50]. In addition, the surface of these planes shows a pattern of striations also known as ridges. These striations correspond to changes in the topography of the fractured surface and are formed by microcracks in the main fracture plane. Generally, its orientation is parallel to the crack growth direction [51].

XRD analyses were also performed on the fracture surfaces to assess the fracture location. Figure 12 shows the X-ray diffraction patterns of multi-material fracture surfaces (control, cross-hatched micropatterns, and circular micropatterns).

By analysing the XRD diffraction patterns, it is possible to verify that in all fracture surfaces, characteristic WC peaks are identified. However, it is possible to observe a variation in the intensity of the peaks and a slight shift to the left of the diffraction pattern peaks of the textured fracture surfaces compared to the characteristic WC peaks. This variation in intensity can be due to the topography of the surfaces and the preferential orientation of the atoms in the planes corresponding to the peaks. The presence of irregularities on the surfaces may have led to the formation of distortions that consequently affect the intensity of the peaks. On the other hand, a preferential orientation in the planes can also influence the peaks intensity, that is, a peak with greater intensity may present a greater preferential orientation of the atoms in the plane corresponding to the peak [52–54]. Since more energy is required for the failure of the multi-material with textures at the interface, it is possible that the slight displacement of the peaks to smaller angles could be due to a possible expansion of the crystal lattice resulting from the formation of stresses during the fracture process of the multi-material [55].

In the diffraction patterns of the fracture surfaces of the textured multi-materials, only WC characteristic peaks were identified, which suggests that the fracture occurred in the WC–Co material, allowing to explain the brittle fracture seen in Fig. 11 b) and c). The reason for the fracture occurring on the WC–Co side is the non-linear fracture path caused by textures at the bonding interface [36], thus indicating that a sound and strong joint was achieved.

Fig. 11 SEM images of multi-material fracture surfaces on the WC–Co side. **a**) control; **b**) cross-hatched micropatterns (experiment VI) and **c**) circular micropatterns (experiment VI)
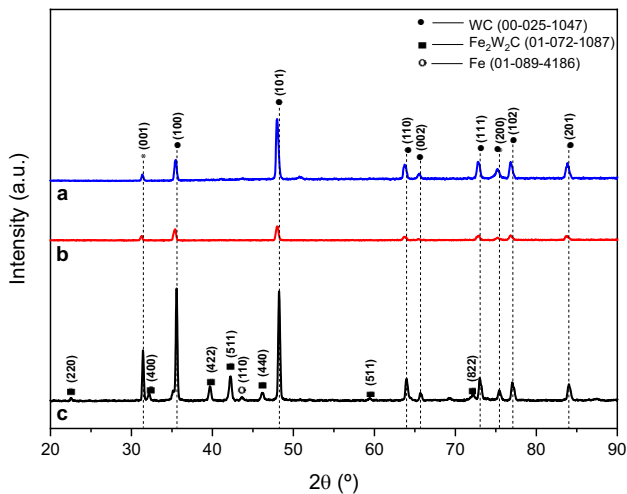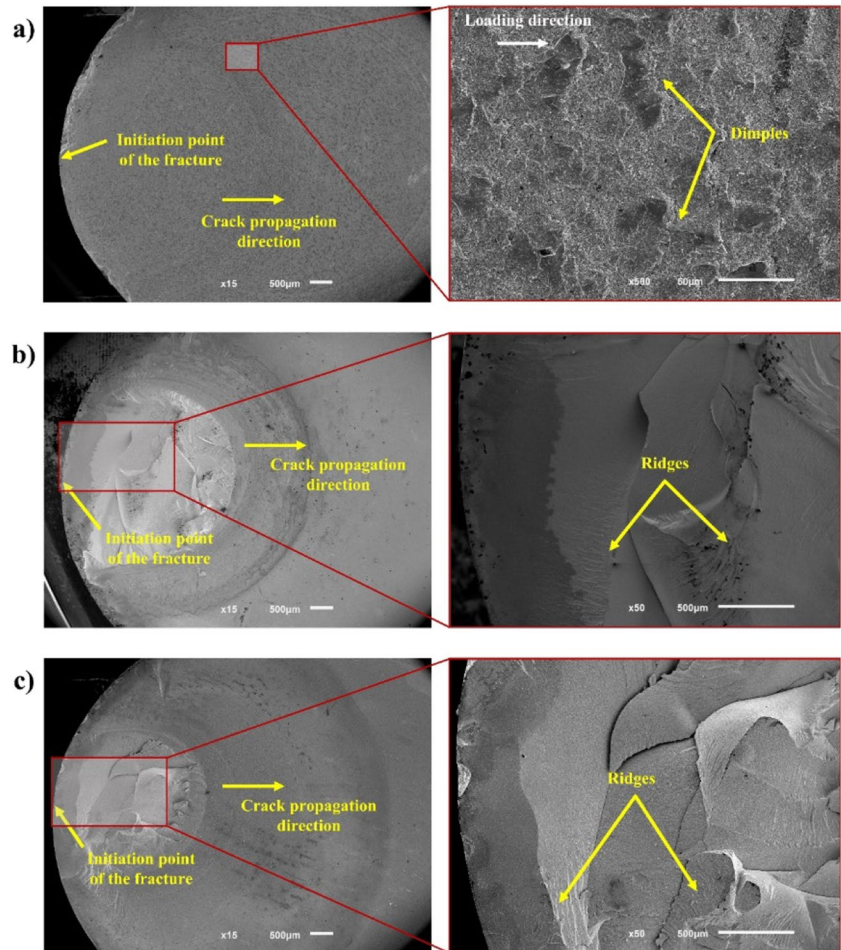
Fig. 12 X-ray diffraction patterns of multi-material fracture surface (WC–Co side): **a**) multi-material with circular micropatterns (experiment VI); **b**) multi-material with cross-hatched micropatterns (experiment VI) and **c**) control specimen

On the other hand, on control specimens surface fracture, in addition to the WC phase peaks, it is also possible to identify the presence of Fe (austenite) and Fe_2W_2C phases. These phases result from the diffusion between 316L SS and WC–Co and their presence on the fracture surface suggests that the fracture of the untextured multi-material (control) has occurred close to the bonding interface, which explains the ductile fracture, as seen in Fig. 11 a). The reason for the fracture occurring on the bonding interface is due to poor contact between the surfaces of the materials, which affects the bonding and leads to the formation of microvoids, consequently impairing the adhesion between WC–Co and 316L SS. Furthermore, since in the textured multi-material there is a greater surface area at the bonding interface where chemical bonds can be established, residual stresses due to CTE mismatch can be reduced due to the presence of a diffusion layer that promotes an intimate bond between WC–Co and the 316L SS [12, 37]. This fact demonstrates that despite the potential formation of the fragile Fe_2W_2C phase at the textured interface, the shear bond strength appears not to be affected, as the fracture occurred in the WC–Co material and not on the interface. Thus, it seems that the textures have a

greater influence than the existence of brittle phases on the bonding strength.

Different studies addressing the bonding of WC–Co to steel report the formation of different brittle phases at the bonding interface, namely, W_4Co_2C, Fe_3W_3C, and Co_3W_3C [13, 21, 56–58]. Luo et al. [59] and Chen et al. [60] reported the formation of the Fe_2W_2C phase at the bonding interface between WC and Fe, and it is described as a fragile phase. In another study, Cai et al. [61] concluded that the formation of the Fe_2W_2C phase depends considerably on carbon diffusion and occurs with lower carbon content.

For bonding interface characterization, the fracture surface (WC–Co side) of the textured multi-materials was cut to obtain a cross-sectional surface. The microstructure and the bonding interface were characterized using SEM and for quantitative analysis of the phases present in the bonding interface, XRD was also used. Figure 13 presents the microstructure of the WC–Co/316L SS bonding joint and the corresponding XRD patterns for the multi-material with cross-hatched and circular micropatterns, showing that bonding joints were successfully formed between WC–Co and 316L SS. The processing conditions that were used resulted in the formation of a wavy-shaped and irregular bonding interface,

where an interdiffusion bond was formed without the presence of microstructural defects, such as microcracks or voids.

In the bonding interface with cross-hatched micropatterns (Fig. 13 a)), we can identify the presence of three regions, namely, a lighter region (WC–Co), a darker region (316L SS), and an interdiffusion zone located between the WC–Co and the 316L SS. On the other hand, for the circular micropatterns (Fig. 13 b)) we can identify a bonding interface similar to the one shown in Fig. 13 a), with an intermediate layer (≈ 4.0 μm) of different microstructure also being observed between the WC–Co and the interdiffusion zone. Some studies on the bonding of WC–Co to steel report the presence of a similar, which is called the transitional layer and generally consists of WC, Co, Fe, and Ni. This transitional layer is characterized by dispersion and increase in the relative separation of WC particles and substitution of Co by elements such as Fe (from steel) and Ni (from an interlayer used for the WC–Co/steel bond) [10, 62–64]. Since this transitional layer is only verified at the circular micropatterns interface, its formation may be associated with the higher energy necessary to produce the circular micropatterns, due to the very localized laser energy in the design of the circles, that leads to localized loss of Co that is then replaced
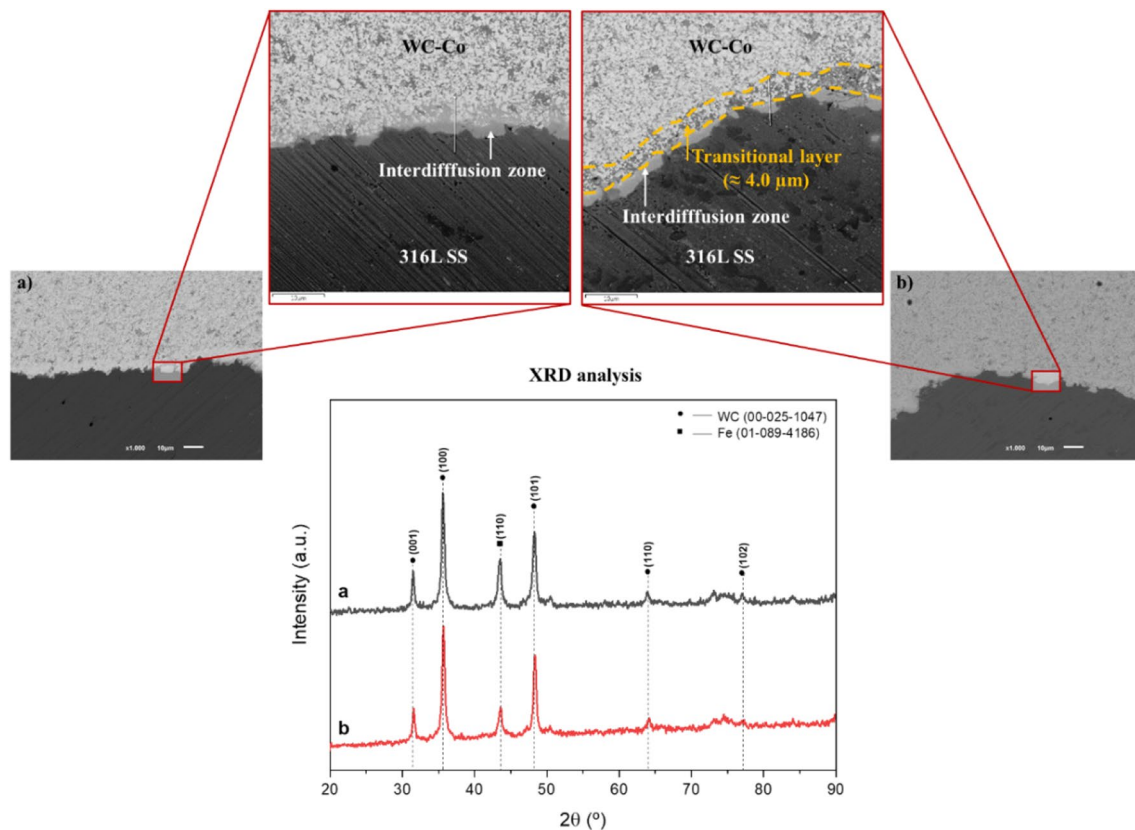
Fig. 13 Cross-section SEM images of WC–Co/316L SS bonding interface and XRD diffraction patterns. **a**) cross-hatched micropatterns (experiment VI) and **b**) circular micropatterns (experiment VI)
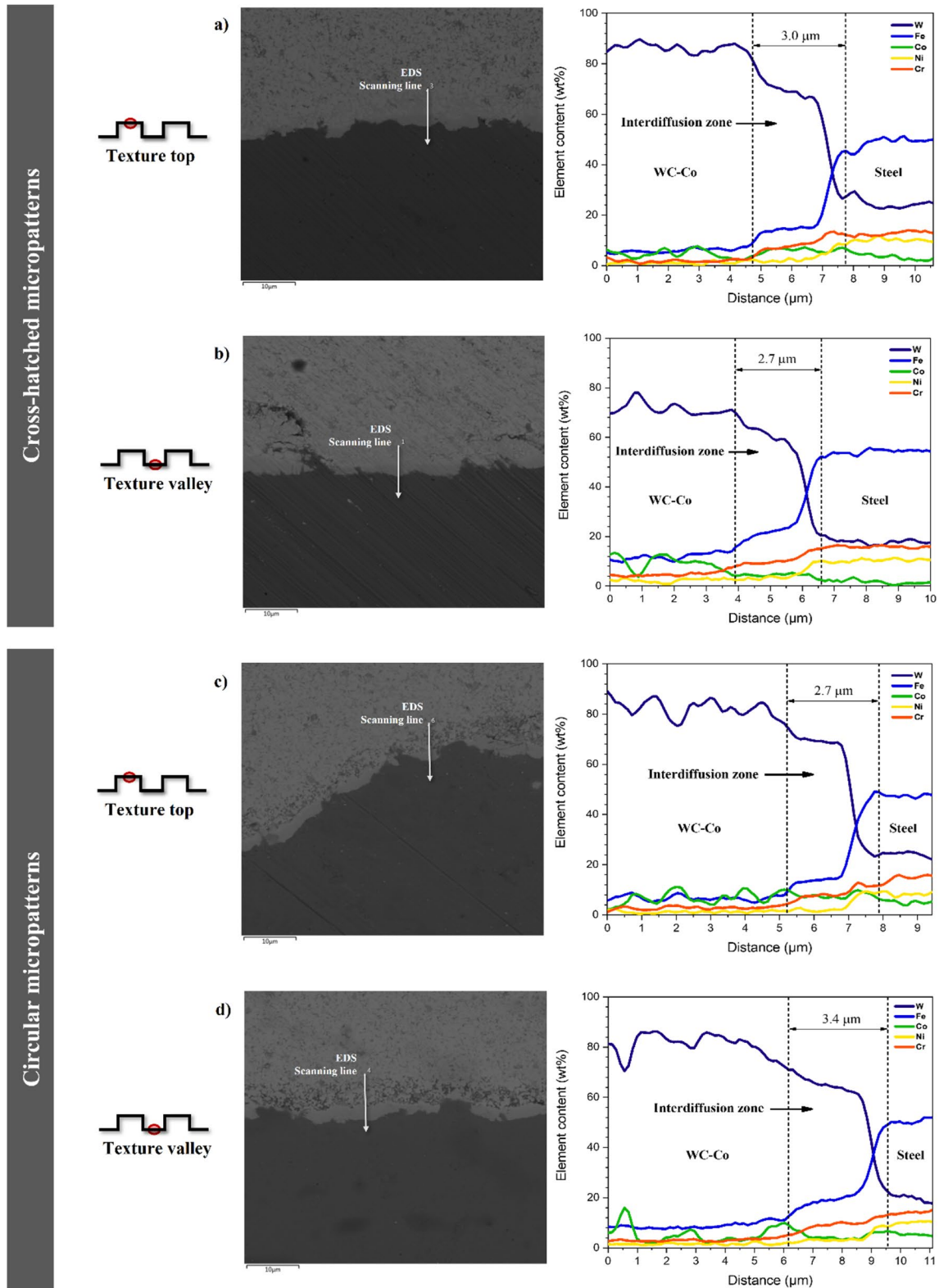
Fig. 14 EDS line analysis and scan direction at the WC–Co/316L SS interface with textures. Cross-hatched micropatterns: **a**) texture top and **b**) texture valley). Circular micropatterns: **c**) texture top and **d**) texture valley

by Fe during the multi-material fabrication [25, 26]. This transitional layer may be the reason why circular micropatterns exhibit a lower shear bond strength when compared to cross-hatched micropatterns.

The XRD diffraction patterns presented in Fig. 13 identify the presence of WC and Fe (austenite) phases. The formation of brittle intermetallic compounds at the bonding interface is not found, probably due to being a very small amount, since an interdiffusion zone is observable in the SEM images.

A quantitative analysis of the distribution of elements in the bonding interface of the WC–Co/316L SS was performed using an EDS scanning line. Figure 14 shows scanning lines results of the WC–Co/316L SS cross-hatched micropatterns top and valley, and circular micropatterns top and valley bonding interface, respectively. First, it is worth noting that for both textures at the bonding interface there was an interdiffusion between WC–Co and 316L SS. On the WC–Co side, there is the presence of a higher content of W and Co and minimum content of Fe. On the other hand, on the 316L SS side, there is the presence of a higher Fe content, an average content of W, Cr, Ni, and minimum content of Co. Along the bonding interface, W content gradually decreases toward the steel, while the Fe content gradually increases towards the steel. Furthermore, a gradual increase of Cr and Ni content (steel alloying elements) towards the steel and a variation of Co content (from WC–Co) can be verified along the bonding interface. This chemical composition gradient at the bonding interface forms an interdiffusion zone of about 2.9 μm (for cross-hatched micropatterns) and 2.7 μm (for circular micropatterns), which contributes to stress relaxation at the bonding interface and for a successful bonding between WC–Co and 316L SS.

The formation of the composition gradient along the bonding interface results from the type of sintering that occurs at the bonding interface. In this case, the sintering of the 316L SS is solid-phase sintering, since the sintering temperature (1100 °C) is lower than its melting point ($\approx$ 1400 °C) [11]. However, according to the Co-Fe equilibrium phase diagram, at 1100 °C, there is the presence of a liquid phase [65]. Therefore, at the beginning of the sintering process, the elements W, Fe, Cr, Co, and Ni contact with each other at the WC–Co/steel bonding interface and the liquid phase is formed. This liquid phase increases with the diffusion of each element (from the WC–Co and the steel) to the liquid zone. The liquid Fe phase diffuses into the WC–Co region, replacing part of the Co. At the same time, WC particles migrate from the WC–Co region to the liquid zone and disperse in the liquid. Furthermore, the liquid Co phase diffuses from the WC–Co region to the steel region due to the high solubility between Fe and Co. After the sintering process, the liquid zone solidifies and the interdiffusion zone and transitional layer are formed [63]. Furthermore, there were no significant differences between the scanning line results for the top and the valley of the textures.

4 Conclusions

In this study, laser surface texturing and pressure-assisted sintering were used to improve the bonding between WC–Co and 316L SS. Laser surface texturing of WC–Co green compacts showed to be effective for producing well defined, non-distorted, reproducible, and equally spaced cross-hatched and circular micropatterns, without compromising the integrity and mechanical strength of these compacts. The bonding between WC–Co and 316L SS was successfully performed using HP at a temperature of 1100 °C, 30 min of sintering and 45 MPa of pressure, being formed an interdiffusion zone, without the presence of microstructural defects and detrimental compounds. Texture dimensions were found to affect the multi-material shear bond strength, with deeper micropatterns having the tendency to lead to lower bonding strength. Overall, the addition of textures at the bonding interface showed a tendency to increase the shear bond strength of the multi-material, with cross-hatched micropatterns generally showing a higher shear strength than circular micropatterns. These results indicate that laser surface texturing and pressure-assisted sintering have the potential to improve the bonding between 316L SS and WC–Co, without needing an interfacial material, thus leading to the development of novel multi-material WC–Co/316L stainless steel cutting tools with enhanced properties and performance. Looking to further enhance the results obtained in this work, additional studies will be performed to understand the shear bond strength variations and influence of different texture designs and dimensions on the bonding between WC–Co and 316L SS. Additionally, a multi-material WC–Co/316L stainless steel cutting tool will be developed, and in-service tests performed to evaluate its machining performance.

Author contributions **Liudmila Basílio:** Conceptualization, Investigation, Writing – original draft, Visualization. **Bruno Guimarães:** Conceptualization, Methodology, Investigation, Writing – review & editing, Supervision. **Óscar Carvalho:** Investigation. **Cristina Fernandes:** Conceptualization, Writing – review & editing. **Daniel Figueiredo:** Resources. **Filipe Silva:** Writing – review & editing, Supervision. **Georgina Miranda:** Conceptualization, Writing – review & editing, Supervision.

Data availability All data used in this work have been properly cited within the article.

Code availability Not applicable.

Declarations

Ethics approval Not applicable.

Consent to participate The authors declare that all authors have read and approved to submit this manuscript to IJAMT.

Consent for publication The authors declare that all authors agree to sign the transfer of copyright for the publisher to publish this article upon on acceptance.

Conflicts of interest/Competing interests The authors declare that they have no known competing financial interests or personal relationships that could have appeared to influence the work reported in this paper.

References

1. Grzesik W (2017) Cutting tool materials. In: Grzesik W (ed) Advanced machining processes of metallic materials, 2nd edn. Elsevier, pp 35–63
2. Guimarães B, Rosas J, Fernandes CM, Figueiredo D, Lopes H, Paiva OC, Silva FS, Miranda G (2023) Real-Time Cutting Temperature Measurement in Turning of AISI 1045 Steel through an Embedded Thermocouple — A Comparative Study with Infrared Thermography. J Manuf Mater Process 7:50. https://doi.org/10.3390/jmmp7010050
3. Enneti RK, Prough KC, Wolfe TA, Klein A, Studley N, Trasorras JL (2018) Sintering of WC-12%Co processed by binder jet 3D printing (BJ3DP) technology. Int J Refract Met Hard Mater 71:28–35. https://doi.org/10.1016/j.ijrmhm.2017.10.023
4. Guimarães B, Silva J, Fernandes CM, Figueiredo D, Carvalho O, Miranda G, Silva FS (2022) Understanding drop spreading behaviour on WC-10wt%Co cutting tools – an experimental and numerical study. Colloids Surf A Physicochem Eng Asp 637:128268. https://doi.org/10.1016/j.colsurfa.2022.128268
5. de Melo ACA, Milan JCG, da Silva MB, Machado ÁR (2006) Some observations on wear and damages in cemented carbide tools. J Brazilian Soc Mech Sci Eng 28:269–277. https://doi.org/10.1590/S1678-58782006000300004
6. Zhang X, Liu G, Tao J, Guo Y, Wang J, Qiao G (2018) Brazing of WC–8Co cemented carbide to steel using Cu–Ni–Al alloys as filler metal: Microstructures and joint mechanical behavior. J Mater Sci Technol 34:1180–1188. https://doi.org/10.1016/j.jmst.2017.11.040
7. Amelzadeh M, Mirsalehi SE (2019) Dissimilar vacuum brazing of cemented carbide to steel using double-layer filler metals. J Manuf Process 47:1–9. https://doi.org/10.1016/j.jmapro.2019.09.015
8. Li SW, Shi JM, Xiong JT, Peng Y, Ren J, Zhang FS, Li J (2021) Microstructural characteristics and mechanical properties of WC-Co/steel joints diffusion bonded utilizing Ni interlayer. Ceram Int 47:4446–4454. https://doi.org/10.1016/j.ceramint.2020.09.157
9. Hidnert P (1934) Thermal expansion of cemented tungsten carbide. J Res Natl Bur Stand 18(1937):47–52. https://doi.org/10.6028/jres.018.025
10. Feng K, Chen H, Xiong J, Guo Z (2013) Investigation on diffusion bonding of functionally graded WC-Co/Ni composite and stainless steel. Mater Des 46:622–626. https://doi.org/10.1016/j.matdes.2012.11.006
11. Aalco - Ferrous and Non-Ferrous Metals Stockist (2020) Grade 316 stainless steel: properties, fabrication and applications. AZoM
12. Feng K, Chen H, Xiong J, Guo Z (2013) Investigation on diffusion bonding of functionally graded WC – Co / Ni composite and stainless steel. Mater Des 46:622–626. https://doi.org/10.1016/j.matdes.2012.11.006
13. Hasan M, Zhao J, Huang Z, Wu H, Jia F, Jiang Z (2019) Effects of Holding Time on the Sintering of Cemented Tungsten Carbide Powder and Bonding with High-Strength Steel Wire. J Mater Eng Perform 28:4074–4085. https://doi.org/10.1007/s11665-019-04153-5
14. Fernandes CM, Oliveira FJ, Senos AMR (2017) Reactive sintering and microstructure development of tungsten carbide-AISI 304 stainless steel cemented carbides. Mater Chem Phys 193:348–355. https://doi.org/10.1016/j.matchemphys.2017.02.030
15. Wang H, Webb T, Bitler JW (2015) Study of thermal expansion and thermal conductivity of cemented WC–Co composite. Int J Refract Met Hard Mater 49:170–177. https://doi.org/10.1016/j.ijrmhm.2014.06.009
16. Amelzadeh M, Mirsalehi SE (2018) Influence of braze type on microstructure and mechanical behavior of WC-Co/steel dissimilar joints. J Manuf Process 36:450–458. https://doi.org/10.1016/j.jmapro.2018.10.015

17. Karimi A, Adeli M, Soltanieh M (2022) Dissimilar joining of cemented carbide to low-carbon steel via combustion welding: Effect of process parameters on the interfacial microstructure and joint strength. J Manuf Process 77:551–560. https://doi.org/10.1016/j.jmapro.2022.03.043

18. Cheniti B, Miroud D, Badji R, Allou D, Csanádi T, Fides M, Hvizdoš P (2017) Effect of brazing current on microstructure and mechanical behavior of WC-Co/AISI 1020 steel TIG brazed joint. Int J Refract Met Hard Mater 64:210–218. https://doi.org/10.1016/j.ijrmhm.2016.11.004

19. Costa AP, Quintino L, Greitmann M (2003) Laser beam welding hard metals to steel. J Mater Process Technol 141:163–173. https://doi.org/10.1016/S0924-0136(02)00954-8

20. Chen G, Shu X, Liu J, Zhang B, Zhang B, Feng J (2019) Electron beam hybrid welding-brazing of WC-Co/40Cr dissimilar materials. Ceram Int 45:7821–7829. https://doi.org/10.1016/j.ceramint.2019.01.088

21. Hasan M, Zhao J, Jia F, Wu H, Ahmad F (2021) Optimisation of sintering parameters for bonding nanocrystalline cemented tungsten carbide powder and solid high strength steel, Compos. Interfaces 28:477–492. https://doi.org/10.1080/09276440.2020.1789537

22. Li S, Li Z, Chen Y, Zu Y, Xiong J, Zhang F, Li J (2022) Microstructural evolution and mechanical properties of diffusion bonding WC-Co cemented carbide to steel using Co and composite Ni/Co interlayers. Int J Refract Met Hard Mater 103:105736. https://doi.org/10.1016/j.ijrmhm.2021.105736

23. Wang X, Zhou D, Xu P (2019) The WC-Co/Fe–Ni interface: Effect of holding time on the microstructure, grain size and grain growth mechanism. Ceram Int 45:23320–23327. https://doi.org/10.1016/j.ceramint.2019.08.031

24. Maizza G, Cagliero R, Iacobone A, Montanari R, Varone A, Mezzi A, Kaciulis S (2016) Study of steel-WC interface produced by solid-state capacitor discharge sinter-welding. Surf Interface Anal 48:538–542. https://doi.org/10.1002/sia.5945

25. Wu C, Guo Z, Liu G, Li Y, Chen L (2021) Effects of groove shape on microstructure and properties of resistance spot welding joints in WC-10Co/B318 steel. Int J Refract Met Hard Mater 101:105693. https://doi.org/10.1016/j.ijrmhm.2021.105693

26. Chen L, Guo Z, Zhang C, Li Y, Wu C, Liu G (2021) Effects of welding current on the microstructure and mechanical behavior of resistance-welded WC-Co/B318 steel joints. Ceram Int 47:17400–17410. https://doi.org/10.1016/j.ceramint.2021.03.056

27. Barrena MI, Gómez de Salazar JM, Matesanz L (2010) Interfacial microstructure and mechanical strength of WC–Co/90MnCrV8 cold work tool steel diffusion bonded joint with Cu/Ni electroplated interlayer. Mater Des 31:3389–3394. https://doi.org/10.1016/j.matdes.2010.01.050

28. Ma B, Wang X, Chen C, Zhou D, Xu P, Zhao X (2019) Dissimilar Welding and Joining of Cemented Carbides. Metals (Basel) 9:1161. https://doi.org/10.3390/met9111161

29. Groover MP (2010) Fundamentals of modern manufacturing: materials, processes and systems, 4th edn. Wiley

30. German RM (2005) Powder Metallurgy and Particulate Materials Processing. MPIF, U.S.A New Jersey

31. Nygren M, Shen Z (2012) Hot pressing and spark plasma sintering. In: Riedel R, Chen I (eds) Ceramics science and technology, 1st edn. Wiley, pp 189–214

32. Maressa P, Anodio L, Bernasconi A, Demir AG, Previtali B (2014) Effect of surface texture on the adhesion performance of laser treated Ti6Al4V alloy. J Adhes 91:518–537. https://doi.org/10.1080/00218464.2014.933809

33. Zhang XM, Yue TM, Man HC (1997) Enhancement of ceramic-to-metal adhesive bonding by excimer laser surface treatment. Mater Lett 30:327–332. https://doi.org/10.1016/S0167-577X(96)00229-7

34. Baburaj EG, Starikov D, Evans J, Shafeev GA, Bensaoula A (2007) Enhancement of adhesive joint strength by laser surface modification. Int J Adhes Adhes 27:268–276. https://doi.org/10.1016/j.ijadhadh.2006.05.004

35. Garcia-Alonso D, Serres N, Demian C, Costil S, Langlade C, Coddet C (2011) Pre-/during-/post-laser processes to enhance the adhesion and mechanical properties of thermal-sprayed coatings with a reduced environmental impact. J Therm Spray Technol 20:719–735. https://doi.org/10.1007/s11666-011-9629-x

36. Wagner WC, Asgar K, Bigelow WC, Flinn RA (1993) Effect of interfacial variables on metal-porcelain bonding. J Biomed Mater Res 27:531–537. https://doi.org/10.1002/jbm.820270414

37. Henriques B, Faria S, Soares D, Silva FS (2013) Hot pressing effect on the shear bond strength of dental porcelain to CoCrMoSi alloy substrates with different surface treatments. Mater Sci Eng C 33:557–563. https://doi.org/10.1016/j.msec.2012.10.001

38. Li L, Xia H, Tan C, Ma N (2018) Effect of groove shape on laser welding-brazing Al to steel. J Mater Process Technol 252:573–581. https://doi.org/10.1016/j.jmatprotec.2017.10.025

39. Chryssolouris G, Stavropoulos P, Salonitis K (2013) Process of Laser Machining. In: Nee A (ed) Handbook of Manufacturing Engineering and Technology. Springer, London, pp 1–25

40. Guimarães B, Figueiredo D, Fernandes CM, Silva FS, Miranda G, Carvalho O (2019) Laser machining of WC-Co green compacts for cutting tools manufacturing. Int J Refract Met Hard Mater 81:316–324. https://doi.org/10.1016/j.ijrmhm.2019.03.018

41. Enomoto T, Sugihara T (2010) Improving anti-adhesive properties of cutting tool surfaces by nano-/micro-textures. CIRP Ann 59:597–600. https://doi.org/10.1016/j.cirp.2010.03.130

42. Kromer R, Costil S, Cormier J, Courapied D, Berthe L, Peyre P, Boustie M (2015) Laser surface patterning to enhance adhesion of plasma sprayed coatings. Surf Coat Technol 278:171–182. https://doi.org/10.1016/j.surfcoat.2015.07.022

43. Guimarães B, Fernandes CM, Figueiredo D, Carvalho O, Silva FS, Miranda G (2020) Effect of laser surface texturing on the wettability of WC-Co cutting tools. Int J Adv Manuf Technol 111:1991–1999. https://doi.org/10.1007/s00170-020-06155-3

44. Bartolomeu F, Buciumeanu M, Pinto E, Alves N, Carvalho O, Silva FS, Miranda G (2017) 316L stainless steel mechanical and tribological behavior—A comparison between selective laser melting, hot pressing and conventional casting. Addit Manuf 16:81–89. https://doi.org/10.1016/j.addma.2017.05.007

45. Miranda G, Faria S, Bartolomeu F, Pinto E, Madeira S, Mateus A, Carreira P, Alves N, Silva FS, Carvalho O (2016) Predictive models for physical and mechanical properties of 316L stainless steel produced by selective laser melting. Mater Sci Eng A 657:43–56. https://doi.org/10.1016/j.msea.2016.01.028

46. Fan X, He D, Wang P, Li D, Liu Y, Ma D, Du Y, Gao S, Kou Z (2016) High pressure infiltration sintering behavior of WC-Co alloys. High Press Res 36:585–594. https://doi.org/10.1080/08957959.2016.1221950

47. Cunha A, Ferreira R, Trindade B, Silva FS, Carvalho O (2020) Production of a laser textured 316L stainless steel reinforced with CuCoBe + diamond composites by hot pressing: Influence of diamond particle size on the hardness and tribological behaviour. Tribol Int 146:106056. https://doi.org/10.1016/j.triboint.2019.106056

48. Chen G, Zhang Y, Huang R, Guo F, Zhang G (2015) Failure mechanism of rock bridge based on acoustic emission technique. J Sensors 2015:1–11. https://doi.org/10.1155/2015/964730

49. Askeland DR, Fulay PP, Wright WJ (2010) The science and engineering of materials, 6th edn. CL-Engineering

50. Shokrian MD, Shelesh-Nezhad K, Najjar R (2019) Effect of CNT dispersion methods on the strength and fracture mechanism of interface in epoxy adhesive/Al joints. J Adhes Sci Technol 33:1394–1409. https://doi.org/10.1080/01694243.2019.1595304

51. González-Velázquez JL (2018) Fractography and failure analysis, 1st edn. Springer, Cham

52. Newbury DE (2004) Quantitative electron probe microanalysis of rough targets: Testing the peak-to-local background method. Scanning 26:103–114. https://doi.org/10.1002/sca.4950260302

53. Zhou J, Wang H (2003) The physical meanings of 5 basic parameters for an X-ray diffraction peak and their application, Chinese. J Geochem 22:38–44. https://doi.org/10.1007/bf02831544

54. Hansford GM, Turner SMR, Degryse P, Shortland AJ (2017) High-resolution X-ray diffraction with no sample preparation. Acta Crystallogr Sect A Found Adv 73:293–311. https://doi.org/10.1107/S2053273317008592

55. Al-Haj Husain N, Camilleri J, Özcan M (2016) Effect of polishing instruments and polishing regimens on surface topography and phase transformation of monolithic zirconia: An evaluation with XPS and XRD analysis. J Mech Behav Biomed Mater 64:104–112. https://doi.org/10.1016/j.jmbbm.2016.07.025

56. Hasan M, Zhao J, Huang Z, Chang L, Zhou H, Jiang Z (2018) Analysis of sintering and bonding of ultra fine WC powder and stainless steel by hot compaction diffusion bonding. Fusion Eng Des 133:39–50. https://doi.org/10.1016/j.fusengdes.2018.05.076

57. Machado IF, Girardini L, Lonardelli I, Molinari A (2009) The study of ternary carbides formation during SPS consolidation process in the WC-Co-steel system. Int J Refract Met Hard Mater 27:883–891. https://doi.org/10.1016/j.ijrmhm.2009.05.001

58. Guimarães B, Guedes A, Fernandes CM, Figueiredo D, Bartolomeu F, Miranda G, Silva FS (2023) WC-Co/316L stainless steel joining by laser powder bed fusion for multi-material cutting tools manufacturing. Int J Refract Met Hard Mater 112:106140. https://doi.org/10.1016/j.ijrmhm.2023.106140

59. Luo J, Wei Z, Xu J, Deng L (2011) Microstructure and properties of microwave sintered 40 wt. % WC steel-bonded carbides. Adv Mater Res 335–336:836–840. https://doi.org/10.4028/www.scientific.net/AMR.335-336.836

60. Chen H, Gu D, Kosiba K, Lu T, Deng L, Xi L, Kühn U (2020) Achieving high strength and high ductility in WC-reinforced iron-based composites by laser additive manufacturing. Addit Manuf 35:1–10. https://doi.org/10.1016/j.addma.2020.101195

61. Cai X, Xu Y, Liu M, Zhong L (2018) Evaluation of microstructure and growth kinetics of tungsten carbide ceramics at the interface of iron and tungsten. J Alloys Compd 741:666–676. https://doi.org/10.1016/j.jallcom.2018.01.212

62. Maizza G, Pero R, De Marco F, Ohmura T (2020) Correlation between the indentation properties and microstructure of dissimilar capacitor discharge welded WC-Co/high-speed steel joints. Materials (Basel). 13. https://doi.org/10.3390/ma13112657

63. Chen H, Feng K, Xiong J, Luo J, Guo Z, Wang H (2012) Characterization and forming process of a functionally graded WC–Co/Ni composite. Int J Refract Met Hard Mater 35:306–310. https://doi.org/10.1016/j.ijrmhm.2012.04.014

64. Chen H, Feng K, Xiong J, Guo Z (2013) Characterization and stress relaxation of the functionally graded WC-Co/Ni component/stainless steel joint. J Alloys Compd 557:18–22. https://doi.org/10.1016/j.jallcom.2012.12.152

65. Okamoto H (2008) Co-Fe (Cobalt-Iron). J Phase Equilibria Diffus 29:383–384. https://doi.org/10.1007/s11669-008-9345-5